Inorganic Chemistry

Article

pubs.acs.org/IC

X-ray Characterization, Electronic Band Structure, and Thermoelectric Properties of the Cluster Compound $Ag_2Tl_2Mo_9Se_{11}$

Rabih Al Rahal Al Orabi,[†] Patrick Gougeon,*[,†] Philippe Gall,[†] Bruno Fontaine,[†] Régis Gautier,[†] Malika Colin,[‡] Christophe Candolfi,[‡] Anne Dauscher,[‡] Jiri Hejtmanek,[§] Bernard Malaman,[‡] and Bertrand Lenoir[‡]

[†]Institut des Sciences Chimiques de Rennes, UMR 6226 CNRS—Ecole Nationale Supérieure de Chimie de Rennes—INSA, Université de Rennes 1, Avenue du Général Leclerc, 35042 Rennes, France

[‡]Institut Jean Lamour, UMR 7198, CNRS—Université de Lorraine, Parc de Saurupt, CS 50840, 54011 Nancy, France

[§]Institut of Physics, Academy of Sciences of the Czech Republic, Cukrovarnicka 10, CZ-162 53 Praha 6, Czech Republic

Supporting Information

ABSTRACT: We report on a detailed investigation of the crystal and electronic band structures and of the transport and thermodynamic properties of the Mo-based cluster compound $Ag_2Tl_2Mo_9Se_{11}$. This novel structure type crystallizes in the trigonal space group $R\bar{3}c$ and is built of a three-dimensional network of interconnected Mo_9Se_{11} units. Single-crystal X-ray diffraction indicates that the Ag and Tl atoms are distributed in the voids of the cluster framework, both of which show unusually large anisotropic thermal ellipsoids indicative of strong local disorder. First-principles calculations show a weakly dispersive band structure around the Fermi level as well as a semiconducting ground state. The former feature naturally explains the presence of both hole-like and electron-like signals observed in Hall effect. Of particular interest is the very low thermal conductivity that remains quasi-constant between 150 and 800 K at a value of approximately 0.6 $W \cdot m^{-1} \cdot K^{-1}$. The lattice thermal conductivity is close to its minimum possible value, that is, in a regime where the phonon mean free path nears the mean interatomic distance. Such extremely low values likely originate from the disorder induced by the Ag and Tl atoms giving rise to strong anharmonicity of the lattice vibrations. The strongly limited ability of this compound to transport heat is the key feature that leads to a dimensionless thermoelectric figure of merit ZT of 0.6 at 800 K.

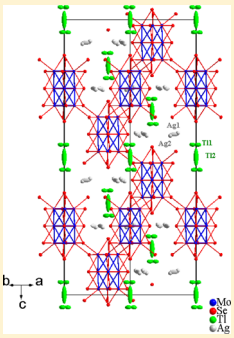

INTRODUCTION

Since the discovery of the Chevrel phases of general formula $M_xMo_6X_8$ (M = transition metals or rare earth, x varying between 0 and 4, and X = S, Se, or Te),[1,2] several other Mo-based cluster compounds were successfully synthesized.[3−13] This general family of materials has rapidly grown to be large in size, with building block units ranging from Mo_6 up to Mo_{36} clusters.[3−13] All the resulting families share the key feature of a three-dimensional network of Mo−X atoms leaving voids that can be filled with a plethora of different species such as alkali, alkaline-earth or rare-earth metals. By varying the size and the geometry of the clusters and the nature of the filler elements, the physical properties may harbor unconventional behavior such as superconductivity coexisting with antiferromagnetic order, two-gap superconductivity or nearly one-dimensional transport properties.[14−18] The complexity of the crystal structure that grows with the nuclearity of the cluster unit suggests that low thermal conductivity values κ may be achieved, opening a new avenue for the search of efficient thermoelectric materials. This last property is one of the prerequisite a material should meet to be a good candidate for thermoelectric applications. This fact is quantified through the dimensionless thermoelectric figure of merit $ZT = \alpha^2T/\rho\kappa$, where T is the absolute temperature, α is the thermopower, ρ is the electrical resistivity, and κ is the total thermal conductivity.[19,20]

Recent investigations on the $Ag_xMo_9Se_{11}$ ($3.4 \le x \le 3.9$) and $Ag_3In_2Mo_{15}Se_{19}$ compounds confirmed this potential by revealing very low κ values both at low and high temperatures.[21−23] In both cases, κ reaches the minimum thermal conductivity, that is, a regime where phonons are scattered so frequently that their mean free path is reduced to the interatomic distance.[21,23] In $Ag_xMo_9Se_{11}$, the possibility to tune the electrical properties from metallic to semiconducting by varying x enabled optimizing the carrier concentration and hence the power factor α^2/ρ.[21,22] The combination of these properties resulted in interesting ZT values at high temperatures with a maximum of 0.65 at 800 K for x = 3.9.[21]

In a continuing effort to explore these families of compounds, we tried to partially substitute Tl for Ag in $Ag_xMo_9Se_{11}$. This choice was dictated both by fulfilling the requirement of replacing monovalent Ag by atoms of similar valence and by several studies demonstrating that Tl-containing compounds may display extremely low κ values.[24−26] Though the $Ag_2Tl_2Mo_9Se_{11}$ compound was obtained in pure form, X-ray diffraction on powders and single crystals revealed that this

Received: August 11, 2014
Published: October 22, 2014

material does not crystallize in the orthorhombic space group *Cmcm* as expected but with a novel structure type of rhombohedral symmetry, successfully indexed in the $R\bar{3}c$ space group.

Here, we report a detailed study of the crystal and electronic structures along with the transport properties in a broad temperature range (2−800 K) of polycrystalline $Ag_2Tl_2Mo_9Se_{11}$. The paper is organized in the following way. After presenting the experimental and computational methods, we describe in detail the room-temperature crystal structure. We then turn to the study of the evolution of the crystallographic parameters upon cooling paying a particular attention to the thermal displacement parameters of the Ag and Tl atoms. The following section deals with the description of the electronic dispersion curves and densities of states. The final section is dedicated to the transport and thermodynamic properties with the aim of determining the interplay between structural, electronic and thermal properties.

EXPERIMENTAL AND COMPUTATIONAL DETAILS

Synthesis. The precursor materials $MoSe_2$, TlSe, Ag, and Mo were used in powder form for solid-state syntheses. In an initial step, Mo powder was reduced under flowing H_2 gas at 1000 °C during 10 h to eliminate traces of oxygen. The binaries $MoSe_2$ and TlSe were obtained by heating stoichiometric mixtures of the elements in sealed evacuated silica tubes during ∼2 d at 800 and 400 °C, respectively. All starting reagents were found monophasic on the basis of their powder X-ray diffraction (PXRD) pattern collected on a D8 Bruker Advance diffractometer equipped with a LynxEye detector (Cu Kα_1 radiation). All the starting reagents were kept and handled in a purified argon-filled glovebox to avoid possible contamination by oxygen and moisture. Single crystals of $Tl_2Mo_9Se_{11}$ were prepared from a mixture of $MoSe_2$, TlSe, and Mo with the nominal composition $Tl_2Mo_{12}Se_{14}$. The initial mixture (ca. 5 g) was cold-pressed and loaded into a molybdenum crucible, which was sealed under a low argon pressure using an arc welding system. The charge was heated at the rate of 300 °C/h to 1500 °C, held at this temperature for 48 h, then cooled to 1000 °C at 100 °C/h, and finally furnace cooled.

Single crystals of $Ag_{\sim 2}Tl_{\sim 2}Mo_9Se_{11}$ were first obtained by an attempt to insert silver atoms in single crystals of the $R\bar{3}$ phase $Tl_{2-x}Mo_9Se_{11}$ ($0 \le x \le 0.4$), whose crystal structure contains an equal mixture of Mo_6Se_8 and $Mo_{12}Se_{11}$ cluster units.[27] The quaternary phase was obtained by reacting directly an excess of silver powder with $Tl_2Mo_9Se_{11}$ single crystals in an evacuated sealed silica tube at 800 °C during two weeks. X-ray investigation performed on one of the silver inserted single crystals revealed that the resulting phase crystallizes in a new structure type based solely on Mo_9Se_{11} cluster unit. The final refined stoichiometry was $Ag_{2.25}Tl_{1.75}Mo_9Se_{11}$. The Ag and Tl contents lead to a cationic charge transfer of +4 toward the Mo_9Se_{11} unit corresponding to the maximum charge transfer toward the Mo_9 cluster. Subsequently, we tried to synthesize polycrystalline samples of nominal compositions $Ag_xTl_{4-x}Mo_9Se_{11}$ with $1 \le x \le 3$ to keep a cationic charge of +4. At 1180 °C, single-phase samples were only observed for $1.9 \le x \le 2.3$ as exemplified by the PXRD pattern of $Ag_2Tl_2Mo_9Se_{11}$ shown in Figure 1. Note that, here, we restrict our investigation on the $x = 2.0$ compound.

Hot Uniaxial Pressing (HUP). The obtained polycrystalline samples of $Ag_2Tl_2Mo_9Se_{11}$ were finely ground into powders and densified by HUP sintering carried out under vacuum (about 10^{-2} mbar). The pressing conditions were the following: the pressure was applied from the beginning of the temperature increase (8 °C/min) to the end of the high-temperature dwell. Typical quantities of 5 g of $Ag_2Tl_2Mo_9Se_{11}$ powders were introduced into a graphite die (Ø 12 mm) previously coated with boron nitride. The applied load was 50 MPa at the beginning of the heating and was gradually increased to 85 MPa when the sintering temperature (1100 °C) was reached. The dwell time was 2 h for all experiments. The densities of the pellets (obtained from measurements of the volume and weight of the pellets) were calculated to be around 98% of the theoretical values.

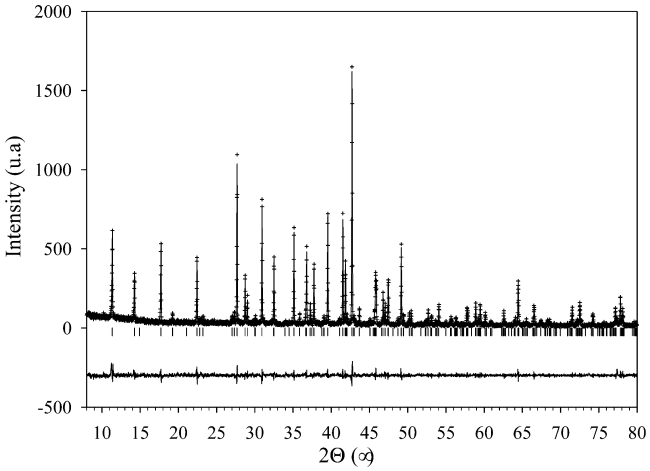

Figure 1. Observed (+), calculated (horizontal line segment) and difference profiles for the refinement of $Ag_2Tl_2Mo_9Se_{11}$ in profile-matching mode (λ = 1.5406 Å).

Single Crystal Structure Determination. A black crystal of dimensions 0.237 × 0.162 × 0.111 mm^3 was selected for further analysis. Intensity data were collected on a Nonius Kappa CCD diffractometer using a graphite-monochromatized Mo Kα radiation (λ = 0.710 73 Å) at room temperature. The COLLECT program package[28] was used to establish the angular scan conditions (φ and ω scans) during the data collection. The data set was processed using EvalCCD for the integration procedure.[29] An absorption correction (T_{min} = 0.0296, T_{max} = 0.1392) was applied using the description of the crystal faces.[30] The structure was successfully solved by direct methods using Sir97[31] and subsequent difference Fourier syntheses in the space group $R\bar{3}c$. All structure refinements and Fourier syntheses were carried out using SHELXL.[32] The first model that includes 2 Mo, 3 Se, 2 Tl, and 1 Ag atoms with site occupancy factors for the Tl and Ag atoms and anisotropic displacement parameters for all atoms was refined down to R = 0.11. At this stage, a difference-Fourier map revealed significant electron densities near the atoms Tl1 (19.63/−10.33 e·Å^{-3}) and Ag1 (3.71/−3.73 e·Å^{-3}). To better describe the electronic density around the Tl1 atom, it was necessary to delocalize the latter around the 3-fold axis. For modeling the silver distribution, it was necessary to introduce a new silver atom Ag2. The residual R value then dropped to 0.0394 and the residual peaks in the vicinity of the Tl1 and Ag atoms to 1.23 and −1.51 e·Å^{-3} and to 1.51 and −0.97 e·Å^{-3}, respectively. The occupancy factors of the Tl and Ag atoms were then refined freely, leading to the final stoichiometry $Ag_{2.251(1)}Tl_{1.749(1)}Mo_9Se_{11}$. Crystallographic data and X-ray structural analysis are summarized in Table 1. The final atomic coordinates, and the equivalent isotropic displacement parameters are gathered in Table 2, and selected interatomic distances are listed in Table 3.

Transport and Thermodynamic Properties Measurements. The samples used for transport properties measurements were cut with a diamond wire saw either into bars or disks (typical dimensions of 2 × 2 × 8 mm^3 and Ø = 10 mm, respectively) depending on the measurement. All the samples were cut perpendicular to the pressing direction.

Low-temperature thermoelectric properties (2−300 K) were measured using the thermal transport option (TTO) of the physical properties measurement system (PPMS, Quantum Design). The contacts were realized by attaching four copper leads onto the sample using conducting silver epoxy. Hall coefficient measurements were conducted between 5 and 300 K on the same sample using the alternating current transport option of the PPMS. A five-probe method was utilized by attaching copper wires with a tiny amount of silver paste. Transverse electrical resistivity ρ_{xy} data were collected while sweeping the magnetic field $\mu_0 H$ from −3 to +3T. The data were

dx.doi.org/10.1021/ic501939k | Inorg. Chem. 2014, 53, 11699−11709

Table 1. Single-Crystal Data Collection and Structure Refinement at 300 K for $Ag_{2.25}Tl_{1.75}Mo_9Se_{11}$

refined composition	$Ag_{2.25}Tl_{1.75}Mo_9Se_{11}$
molar mass (g mol^{-1})	2324.2
symmetry	trigonal
space group	$R\bar{3}c$
a (Å)	10.0180(4)
c (Å)	35.5923(16)
V (Å^3)	3093.5(2)
Z	6
ρ (g·cm^{-3})	7.5002
radiation	Mo Kα
θ range	2.6−34.84°
linear abs. coefficient μ (mm^{-1})	40.156
reflection collected	15 950
reflection unique	1511
number of parameters	62
final R value (%)	0.0393
S (goodness of fit)	1.163

Table 3. Selected Interatomic Distances (in Å) for $Ag_{2.25}Tl_{1.75}Mo_9Se_{11}$

Mo1−Mo1	2.6166(15)	Tl1−Se3	3.0240(15)
Mo1−Mo2	2.6703(6)	Tl1−Se1	3.116(3)
Mo1−Mo2	2.7488(7)	Tl1−Se1	3.345(4)
Mo1−Se3	2.5568(9)	Tl1−Se2	3.391(3)
Mo1−Se1	2.5784(14)	Tl1−Se1	3.722(2)
Mo1−Se1	2.6620(15)	Tl1−Se2	3.829(3)
Mo1−Se1	2.6645(11)	Tl1−Se1	3.881(3)
Mo1−Se2	2.6687(7)	Tl1−Se2	4.169(3)
Mo2−Mo2	2.7339(17)	Tl1−Se1	4.210(3)
Mo2−Se2 (×2)	2.5823(14)	Tl1−Se1	4.382(3)
Mo2−Se1 (×2)	2.6435(7)		
		Tl2−Se1 (×6)	3.4041(7)
		Ag1−Se2	2.569(15)
		Ag1−Se1 (×2)	2.652(8)
		Ag2−Se1	2.663(7)
		Ag2−Se2	2.593(3)
		Ag2−Se1	2.724(6)
		Ag2−Se3	2.966(8)

corrected to dismiss possible magnetoresistive contribution due to contact misalignment following the formula $\rho_H = [\rho_{xy}(+\mu_0 H) - \rho_{xy}(-\mu_0 H)]/2$, where ρ_H is the Hall voltage. Specific heat was measured on a small prism-shaped sample (mass of ∼15 mg) from 0.4 to 4 K and from 2 to 300 K using, respectively, the He3 and He4 options of the PPMS.

High-temperature thermoelectric measurements were carried out in the 300−800 K temperature range. Thermopower and electrical resistivity were measured simultaneously with a ZEM3 system (ULVAC-RIKO) under helium atmosphere on the bar-shaped sample used for TTO and Hall effect measurements. An overall good match between the low- and high-temperature data sets was observed, the deviation being at most 10%.

Thermal diffusivity a was determined in the same temperature range using a Netzsch laser flash instrument (LFA 427). The sample was coated with a thin layer of graphite to favor both absorption and emission. The data were analyzed by the Cowan model including pulse correction. Assuming a constant density ρ_V, the thermal conductivity κ was calculated from $\kappa = aC_p\rho_V$. The specific heat C_p was estimated by the Dulong−Petit law (0.254 J·g^{-1}·K^{-1}). The combined uncertainty in the determination of ZT is estimated to be ∼20%.

The electrical and thermal diffusivity were measured at high temperatures perpendicular and parallel, respectively, to the pressing direction. Given the anisotropic crystal structure (see below), we may expect the transport properties to show some degree of anisotropy as well. The anisotropy can be directly probed through a comparison at room temperature between the low-temperature and high-temperature thermal conductivity data (measured perpendicular and parallel, respectively, to the pressing direction). In fact, they show only a slight mismatch (apart from the thermal radiations that appear near room temperature) suggesting a weak anisotropy. Thus, it can be concluded that the anisotropy does not significantly influence transport in our polycrystalline sample. This conclusion is further corroborated by PXRD measurements, which show no signs of preferred grain orientation after the densification process.

Electronic Band Structure Calculations. Self-consistent *ab initio* band structure calculations were performed on the model compound $Ag_2Tl_2Mo_9Se_{11}$ (see Supporting Information for the structural details) with the scalar relativistic tight-binding linear muffin-tin orbital (LMTO) method in the atomic spheres approximation including combined correction.[33] Exchange and correlation were treated in the local density approximation using the von Barth−Hedin local exchange correlation potential.[34] Within the LMTO formalism, interatomic spaces are filled with interstitial spheres. The optimal positions and radii (r_{ES}) of these additional "empty spheres" (ES) were determined by the procedure described in ref 35. Sixteen non-symmetry-related ES with 0.90 Å ≤ r_{ES} ≤ 1.60 Å were introduced in these calculations. The full LMTO basis set consisted of 5s, 5p, 4d, and 4f functions for Mo and Ag spheres, 6s, 6p, 5d, and 4f for Tl spheres, 4s, 4p, and 4d for Se spheres, and s, p, and d functions for ES. The eigenvalue problem was solved using the following minimal basis set obtained from the Löwdin downfolding technique: Mo 5s, 5p, 4d, Ag 5s, 5p, 4d; Tl 6s, 6p; Se 4s, 4p; and interstitial 1s LMTOs. The k-space integration was performed using the tetrahedron method.[36] Self-consistent charge and averaged properties were obtained from 69 irreducible k points. A measure of the magnitude of the bonding was obtained by computing the crystal orbital Hamiltonian populations (COHP) corresponding to the Hamiltonian population weighted density of states (DOS).[37] As recommended, a reduced basis set (in which all ES LMTOs were downfolded) was used for the COHP

Table 2. Fractional Atomic Coordinates and Equivalent Isotropic Thermal Displacement Parameters (Å^2) for $Ag_{2.25}Tl_{1.75}Mo_9Se_{11}$

atom	Wyckoff position	x	y	z	U_{iso}	s.o.f
Mo1	36f	−0.00896(5)	0.14612(5)	0.18748(2)	0.01648(12)	1
Mo2	18e	0.15757(6)	0.15757(6)	0.25	0.01559(13)	1
Se1	36f	0.28726(6)	0.31485(6)	0.18803(2)	0.02004(13)	1
Se2	18e	0.29747(7)	0	0.25	0.01945(16)	1
Se3	12c	0	0	0.12953(2)	0.02162(19)	1
Ag1	18e	0.5539(4)	0	0.25	0.022(3)	0.1156(2)
Ag2	36f	0.5282(6)	−0.0491(9)	0.2523(2)	0.0416(13)	0.3174(1)
Tl1	36f	0.7217(2)	0.3545(3)	0.28768(3)	0.0535(6)	0.2385(1)
Tl2	6b	0.666 667	0.333 333	0.333 333	0.314(18)	0.3182(6)

dx.doi.org/10.1021/ic501939k | Inorg. Chem. 2014, 53, 11699−11709

calculations. Dispersion curves, DOS and COHP were shifted so that ε_F lies at 0 eV.

RESULTS AND DISCUSSION

Room-Temperature Crystal Structure. $Ag_{2.251(1)}Tl_{1.749(1)}Mo_9Se_{11}$ crystallizes in a new structural type described in the space group $R\bar{3}c$. The crystal structure consists in a three-dimensional framework of Mo−Se atoms forming interconnected $Mo_9Se_{11}Se_6$ clusters as illustrated in Figure 2.

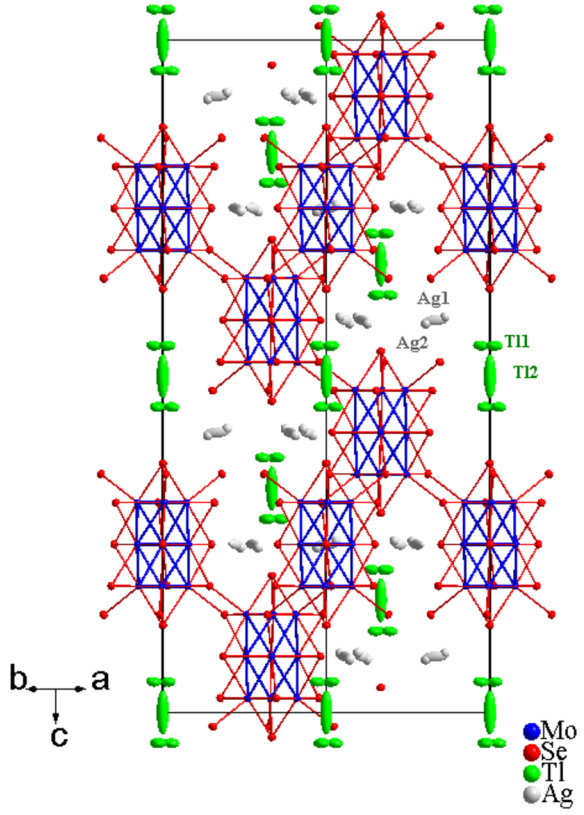

Figure 2. View of the crystal structure of $Ag_{2.25}Tl_{1.75}Mo_9Se_{11}$ along the [110] direction. Ellipsoids are drawn at the 50% probability level.

The $Mo_9Se_{11}Se_6$ unit (Figure 3), centered on the 6*a* position with point symmetry 3 2 or D_3, can be classically described as resulting from the monoaxial face-sharing condensation of two $Mo_6Se_8Se_6$ units with loss of the Se atoms belonging to the shared faces. Another way to describe this unit is by considering the stacking of three planar Mo_3Se_3 with two supplementary Se atoms capping the outer triangular faces. The outer Mo1 and inner Mo2 atoms display different environments. The environment of the former is similar to that encountered in the $Mo_6X_8X_6$ units (X = S, Se) of the rhombohedral MMo_6X_8 compounds.[1] They are surrounded by four Mo atoms (two outer Mo1 and two inner Mo2) and four Se atoms (2 Se1, 1 Se2 and, 1 Se3), in an approximately coplanar coordination, and another Se1 atom belonging to an adjacent Mo_9Se_{11} cluster. This last atom constitutes the apex of a square-based pyramidal environment. The Mo2 atoms of the median Mo_3 triangles are surrounded by six Mo atoms (4 outer Mo1 and 2 inner Mo2) and only four Se atoms (two Se1 and two Se2) belonging to the same cluster unit. As observed in previous Mo-condensed-cluster chalcogenides,[3−13] two kinds of Mo−Mo distances (see Table 3) can be distinguished in the units: the Mo1−Mo1 and Mo2−Mo2 intratriangle distances, 2.6174(8) and 2.7350(8) Å, respectively. These distances correspond to those within the Mo_3 triangles formed by the Mo1 and Mo2 atoms related through the 3-fold axis and the two Mo1−Mo2 distances (2.6704(6) and 2.7490(6) Å) between the Mo_3 triangles. The average Mo−Mo distance is 2.687 Å, that is, slightly shorter than those observed in the compounds $Ag_{2.6}CsMo_9Se_{11}$ and $Ag_{4.1}ClMo_9Se_{11}$ (2.694 and 2.702 Å, respectively), which also contain Mo_9 clusters but crystallize in the $P6_3/m$ space group.[3] This likely reflects the higher cationic charge transfer toward the Mo_9 cluster, which is +4 in $Ag_{2.25}Tl_{1.75}Mo_9Se_{11}$ but only amounts to +3.6 and +3.1 in $Ag_{2.6}CsMo_9Se_{11}$ and $Ag_{4.1}ClMo_9Se_{11}$, respectively. The Mo−Se bond distances are typical, ranging between 2.556(1) and 2.6681(6) Å (see Table 3). Each unit is connected to six adjacent units via 12 interunit Mo1−Se1 bonds of 2.664(1) Å to form a three-dimensional Mo−Se framework in which the shortest intercluster distance is 3.6919(8) Å. The connective formula of the Mo−Se network formed is $[Mo_9Se^{i}_{5}Se^{i\text{-}a}_{6/2}]Se^{a\text{-}i}_{6/2}$ in Schäfer's notation.[38] The Ag1 and Ag2 atoms occupy a distorted trigonal bipyramidal site formed by the Se atoms (Figure 4). The Ag1 atom is located in the mirror plane around the 3-fold axis (18*e* Wyckoff position) and is in triangular environment of Se atoms (one Se2 at 2.553(2) Å and two Se1 at 2.661(1) Å). The Ag2 atom, which is at 0.54 Å from the Ag1 atom, is slightly off the triangle and is surrounded by four Se atoms at distances ranging from 2.599(12) to 2.847(10) Å. The Tl1 and Tl2 atoms occupy the 36*c* and 6*b* Wyckoff positions with site symmetries 1 and −3, respectively. The Tl1 atoms are surrounded by 10 Se atoms forming a distorted tetrahedron (three Se1 and one Se3) whose three faces are capped (three Se2) and three edges bridged (three Se1) (Figure 4). The Tl1−Se range between 3.0239(15) and 4.383(3) Å. Finally, the Tl2 atoms are surrounded by six Se1 atoms at 3.4041(7) Å forming a trigonal antiprism (Figure 4).

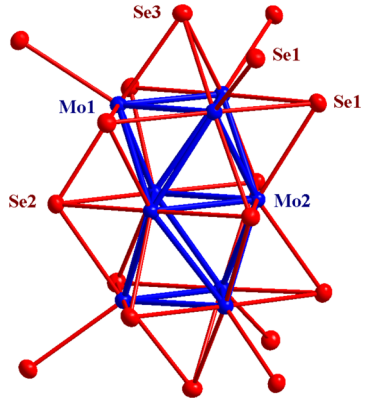

Figure 3. $Mo_9Se_{11}Se_6$ cluster unit (ellipsoids at the 50% probability level).

Low-Temperature Crystal Structure. The structural model used to describe the crystal structure at 300 K could be successfully refined down to 100 K. The results indicate a larger contraction of the unit cell along the *a* direction upon cooling with respect to the *c* axis. An estimate of the linear thermal expansion coefficients in both directions were obtained by applying the relations $\beta_a = (1/a)((\partial a)/(\partial T))$ and $\beta_c = (1/c)((\partial c)/(\partial T))$, yielding 9.7×10^{-6} and 8.5×10^{-6} K^{-1} for β_a and β_c, respectively. The temperature dependences of the equivalent isotropic displacement parameters U_{eq} of the Ag and

dx.doi.org/10.1021/ic501939k | Inorg. Chem. 2014, 53, 11699−11709

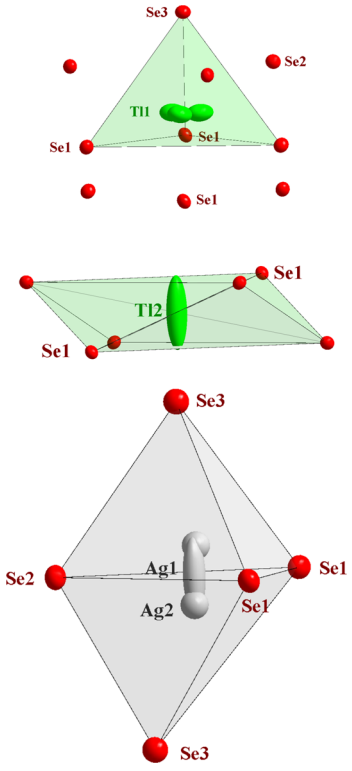

Figure 4. Selenium environments for the Tl and Ag atoms (ellipsoids at the 50% probability level).

Tl atoms are shown in Figure 5. The Ag1 and Tl1 atoms show large U_{eq} values, which decrease only slightly on cooling. These

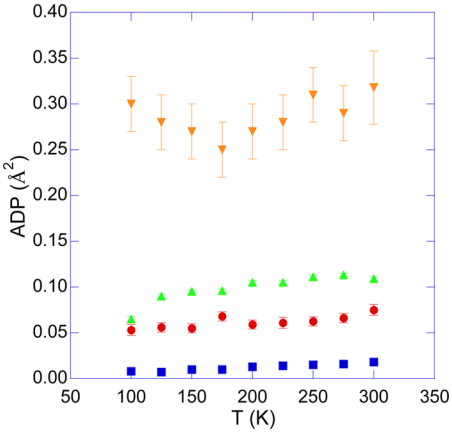

Figure 5. Temperature dependence of the equivalent isotropic displacement parameters of the Ag1 (red ●), Ag2 (blue ■), Tl1 (green ▲), and Tl2 (yellow ▼) atoms.

values are similar to those observed for the Ag atoms in single-crystalline $Ag_{3.6}Mo_9Se_{11}$ for which the ADPs range between 0.030 and 0.074 Å^2.[4] Unlike Ag1 and Tl1 atoms, the apparent U_{eq} for Tl2 is enormous and nearly temperature-independent. This behavior implies an extremely large positional and static disorder given by the magnitude of the low-temperature intercept. These results parallel those observed in clathrates ($X_8Ga_{16}Ge_{30}$ where X = Eu, Sr, Ba) for which, the cations entrapped in the cages show a large static disorder that can be accounted for by a split-site position.[39−43] Because in these compounds the lattice thermal conductivity shows an anomalous glass-like behavior, we may expect the thermal transport in $Ag_2Tl_2Mo_9Se_{11}$ to exhibit similar temperature dependence. As we shall see in the following sections, very low thermal conductivity values are indeed observed.

Electronic Band Structure. The electronic structures of some octahedrally condensed transition-metal M_9 chalcogenide clusters were analyzed in several studies with the aid of extended Hückel and density functional molecular orbital calculations. Some of us showed that the optimal metallic electron (ME) count for a Mo_9Se_{11} unit is equal to 36.[44,45] Higher electron counts suggest the occupation of antibonding levels that should weaken metal−metal bonding. This situation occurs in the isostructural electron-richer $Co_9Se_{11}(PPh_3)_6$ cluster that includes 59 MEs.[46] A previous theoretical analysis of the electronic structure of this cluster revealed that metal−metal bonding is indeed weaker within the metallic M_9 architecture leading to longer Co−Co contacts than in *hcp* Co.[47] Unlike this case, Mo−Mo distances within Mo_9Q_{11} (Q = chalcogen) unit are comparable to those in *bcc* Mo.

Prior studies devoted to Mo_9-based compounds have shown that their electronic structure can be rationalized on the basis of the molecular orbital (MO) diagram of the isolated cluster unit.[3,22] This conclusion holds true for mixed Mo_6 and Mo_9 cluster compounds.[13,48,49] Although molybdenum clusters are connected to each other via shared chalcogen atoms, interactions between neighboring clusters are not strong enough to perturb the MO pattern of the isolated Mo_9 cluster. The MO diagram of an isolated Mo_9Q_{11} shows a significant energy gap that separates Mo−Mo bonding MOs from Mo−Mo antibonding MOs.[45] This gap becomes the highest occupied molecular orbital/lowest unoccupied molecular orbital (HOMO/LUMO) gap for $Mo_9Q_{11}^{4-}$ anions. The LUMO of the $Mo_9Se_{11}^{4-}$ unit is strongly localized on the metal atoms, Mo−Mo antibonding overall, and rather high in energy. Therefore, the optimal ME count of such a unit is equal to 36. Assuming an ionic interaction between the monovalent Tl and Ag atoms and the cluster network, the formal charge of Mo_9Se_{11} and its ME count are equal to −4 and 36, respectively.

Density functional theory (DFT) calculations were carried out on the model compound $Ag_2Tl_2Mo_9Se_{11}$ based on the crystal structure of $Ag_{2.25(1)}Tl_{1.75(1)}Mo_9Se_{11}$. Owing to the partial occupation of silver and thallium sites, the crystal structure of $Ag_2Tl_2Mo_9Se_{11}$ has been described in the $P\bar{3}c1$ space group (No. 165) using the experimental cell parameters of $Ag_{2.25(1)}Tl_{1.75(1)}Mo_9Se_{11}$. The crystal structure of this model includes five Mo, eight Se, three Tl, and one Ag atom sites (see Supporting Information). The electronic structure was computed within the DFT formalism: density of states (DOS) and Mo−Mo COHP are sketched in Figures 6 and 7. The latter was obtained by averaging all COHP computed for Mo−Mo contacts ranging from 2.670 to 2.747 Å. These curves are similar to the one computed for $Ag_3CsMo_9Se_{11}$ (see Figure 7 in ref 3). A significant indirect band gap (its width is computed to 0.55 eV for $Ag_2Tl_2Mo_9Se_{11}$) separates the occupied Mo−Mo bonding bands from the vacant Mo−Mo antibonding bands. The bands in the vicinity of the Fermi level are mainly centered on molybdenum atoms and to a lesser extent on the chalcogens. The computed charges of Ag and Tl are equal to +0.71 and +0.63 in agreement with the major ionic interaction between these elements and the Mo−Se network. Likewise $Ag_3CsMo_9Se_{11}$,[3] the top of the valence band is mainly composed of Mo−Mo bonding states. A higher charge transfer is achieved in the title compound with respect to

dx.doi.org/10.1021/ic501939k | Inorg. Chem. 2014, 53, 11699−11709

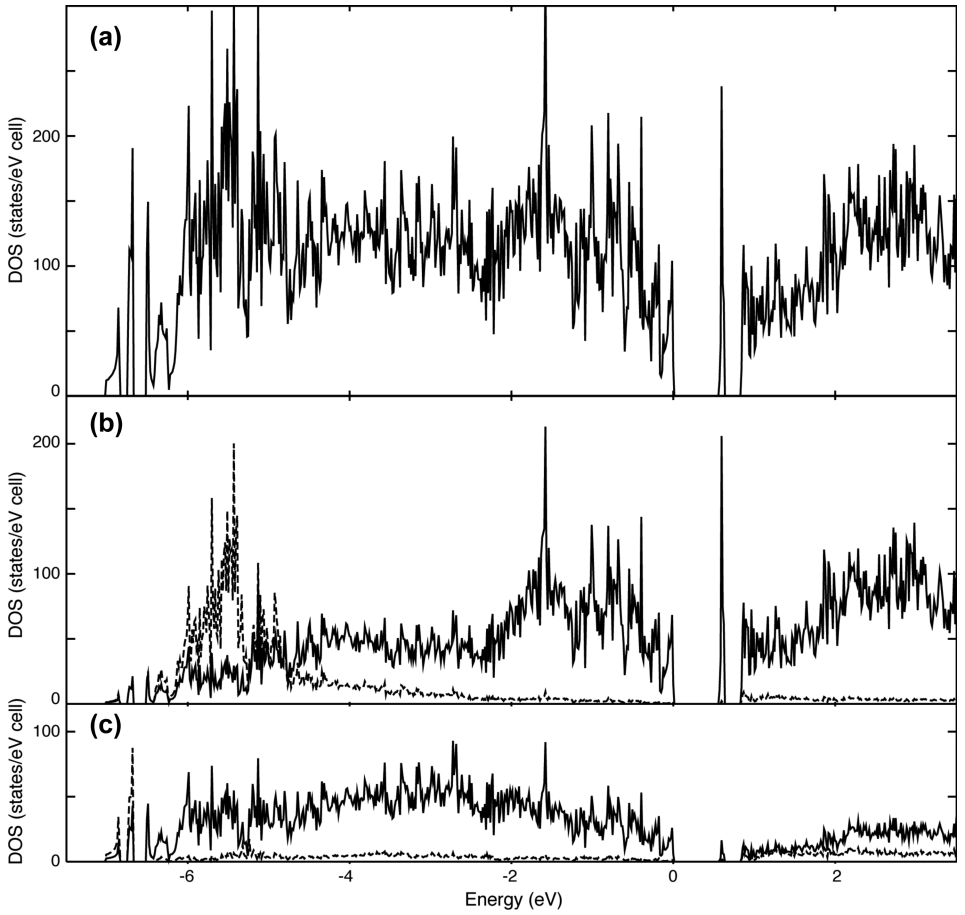

Figure 6. Energy dependence of the DOS for $Ag_2Tl_2Mo_9Se_{11}$: (a) total, (b) Mo (plain) and Ag (dotted) contributions, (c) Se (plain) and Tl (dotted) contributions.

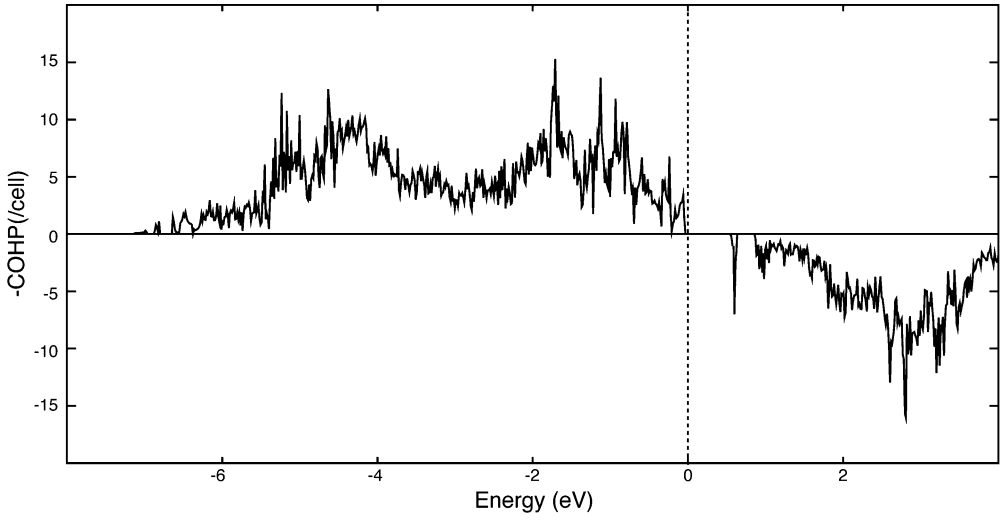

Figure 7. Average Mo−Mo COHP curve computed using Mo−Mo contacts ranging from 2.670 to 2.747 Å for $Ag_2Tl_2Mo_9Se_{11}$.

$Ag_{2.6}CsMo_9Se_{11}$ and $Ag_{4.1}ClMo_9Se_{11}$,[3] which explains the shorter average Mo−Mo distance in $Ag_2Tl_2Mo_9Se_{11}$ (2.685 Å) compared to that found in the two others (2.694 and 2.702 Å, respectively). The electronic band structure of $Ag_2Tl_2Mo_9Se_{11}$ is shown in Figure 8. The Fermi level nears the top of the valence bands indicative of a semiconducting ground state. Likewise the $Ag_xMo_9Se_{11}$ phase, one of the main characteristics is the low dispersion of the bands that originates from a weak interaction between the clusters.

Electronic Transport Properties. Band structure calculations have predicted a semiconducting ground state synonymous of a decrease in the electrical resistivity with temperature. Aside from a more complex behavior below 100 K, our experimental $\rho(T)$ data, shown in Figure 9, confirm this trend. Above 600 K, the $\rho(T)$ values tend to level off and no

dx.doi.org/10.1021/ic501939k | Inorg. Chem. 2014, 53, 11699−11709

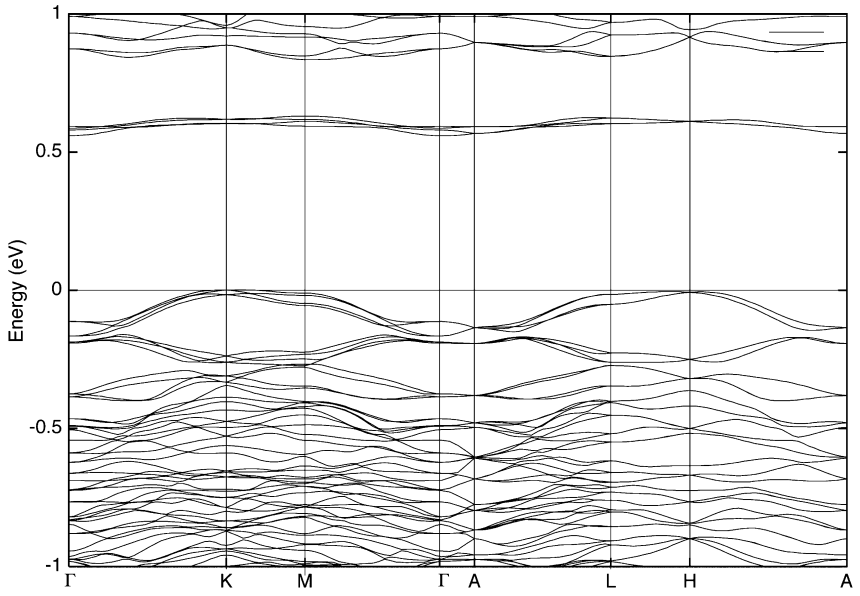

Figure 8. Electronic dispersion curves of $Ag_2Tl_2Mo_9Se_{11}$. The different points have the following coordinates in units of the reciprocal lattice vectors: Γ = (0, 0, 0), K = (1/3, 1/3, 0), M = (1/2, 0, 0), A = (0, 0, 1/2), L = (1/2, 1/2, 0), and H = (1/3, 1/3, 1/2).

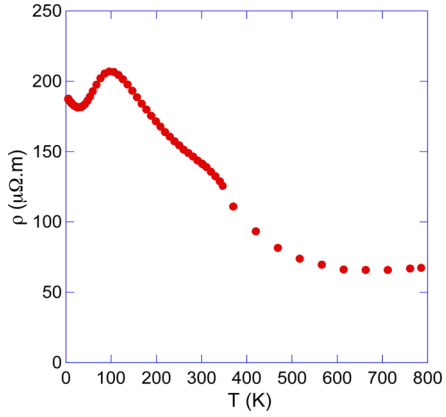

Figure 9. Electrical resistivity as a function of temperature.

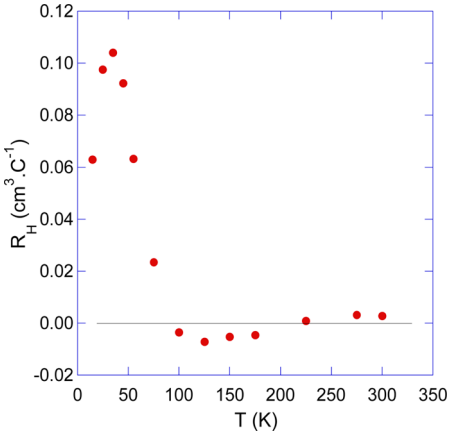

Figure 10. Temperature dependence of the Hall coefficient R_H. The solid black line represents $R_H = 0$ to underline the sign change of R_H.

longer show significant variations up to 800 K. Yet, fitting the data above 100 K to a simple Arrhenius law neither satisfactorily describes $\rho(T)$ nor does it yield a reasonable estimation of the activation energy. Below 100 K, the temperature dependence shows successively a metallic-like and a semiconducting-like behavior upon cooling. A possible origin of this temperature dependence may be related to variations in carrier concentration and/or scattering mechanisms.

To determine whether this possibility is indeed at play, Hall effect measurements were performed down to 5 K. Within the magnetic field range covered, the $\rho_H(\mu_0 H)$ data vary linearly in the whole temperature range (not shown). The sign of the slope however evolves with temperature and two transitions from p- to n-type and then n- to p-type were identified. These transitions are clearly visualized in the Hall coefficient (R_H) data inferred from $((\partial\rho_H)/(\partial(\mu_0 H))|_{\mu_0 H\to 0})$ and shown in Figure 10. The R_H values, positive above 225 K and only weakly temperature-dependent, become negative between 200 and 100 K. Below 100 K, R_H switches back to positive values and shows a steep rise upon further cooling. A maximum is reached at 35 K and the values eventually decrease down to 5 K. The two sign changes indicate that holes (positive R_H) and electrons (negative R_H) alternatively dominate the transport. The strong increase observed below 100 K coincides with the upturn seen in the $\rho(T)$ data suggesting that variations in the carrier concentration directly govern the low-temperature behavior of ρ. The presence of the two types of carriers indicates a multiband character of the transport in this compound. Because of this characteristic, the hole concentration p cannot be simply determined from the conventional relation $R_H = 1/pe$ (e is the elementary charge). Applying this relation only provides an upper limit of the actual p value. What is more surprising from these results is that band structure calculations did not reveal any overlap between the valence and conduction bands, which would naturally explain the presence of both types of carrier. The situation is reminiscent to that observed in the $Ag_xMo_9Se_{11}$ phase ($3.4 \leq x \leq 3.8$) where both carriers were found to compete at low temperatures event though the conduction and valence bands are well separated.[22] Interestingly, these two systems share similar electronic dispersion in the vicinity of the Fermi level with both negative and positive curvatures (see Figure 8). While the former leads to a hole-like signal under

dx.doi.org/10.1021/ic501939k | Inorg. Chem. 2014, 53, 11699−11709

thermal or electric gradient, the latter gives rise to an electron-like contribution observable in the Hall transport. Note that a similar mechanism might be also at play in the cluster compound $Ag_3In_2Mo_{15}Se_{19}$ (ref 23) suggesting that weakly dispersive bands, and hence electron-like and hole-like contributions, may be a quite general feature among Mo-based cluster compounds.

Figure 11 shows the thermopower as a function of temperature. The thermopower values remain large and

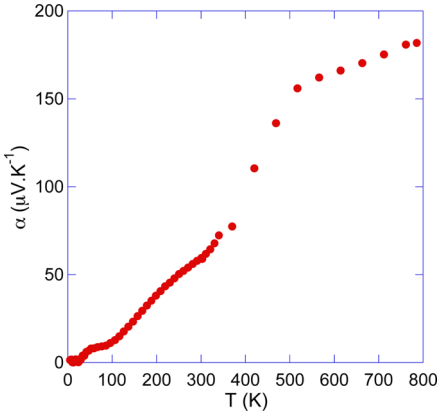

Figure 11. Thermopower as a function of temperature of $Ag_2Tl_2Mo_9Se_{11}$.

positive in the temperature range covered, varying between ~60 $\mu V \cdot K^{-1}$ at 300 K to ~180 $\mu V \cdot K^{-1}$ at 800 K. The low-temperature data are characterized by a maximum near 50 K that may be related to a phonon-drag effect. Above 300 K, a steeper increase in a is observed that becomes less pronounced above 500 K. The nonlinear behavior of α likely reflects the presence of holes and electrons observed in the Hall signal. Both carriers contribute to the thermopower through partial contributions following the two-band formula[50]

$$\alpha = \frac{\alpha_e\sigma_e + \alpha_h\sigma_h}{\sigma_e + \sigma_h} \quad (1)$$

In eq 1, the pairs α_e, α_h and σ_e, σ_h are the partial thermopower and conductivities, respectively, of electrons (e) and holes (h). The stronger rise in temperature suggests that the contribution of holes is dominant at high temperatures. The saturation tendency observed above 500 K may be indicative of either thermal activation of intrinsic carriers or a crossover to a regime where the electron contribution dominates.

Thermal Transport Properties. Figure 12a presents the temperature dependence of the specific heat C_p of $Ag_2Tl_2Mo_9Se_{11}$ measured to 0.4 K. At 300 K, the magnitude of C_p is slightly lower than the Dulong–Petit limit $3NR$, where N is the number of atoms in the formula unit, and R is the ideal gas constant. One of the most intriguing features revealed by these data is the linear-in-T region only visible at low temperatures (below ~2.5 K, see Figure 12b) indicating that the Fermi-liquid formula $C_p/T = \gamma + \beta T^2$ holds in a narrow temperature range. The Sommerfeld coefficient γ and the β parameter standing for the phonon contribution were determined from a linear fit to the data yielding γ = 14.1 mJ $mol^{-1} \cdot K^{-2}$ and β = 46.6 mJ $mol^{-1} \cdot K^{-4}$. Although our first-principles calculations suggested a semiconducting ground state, the experimental γ value rather indicates a finite DOS value at E_F. This discrepancy may have several origins. On one

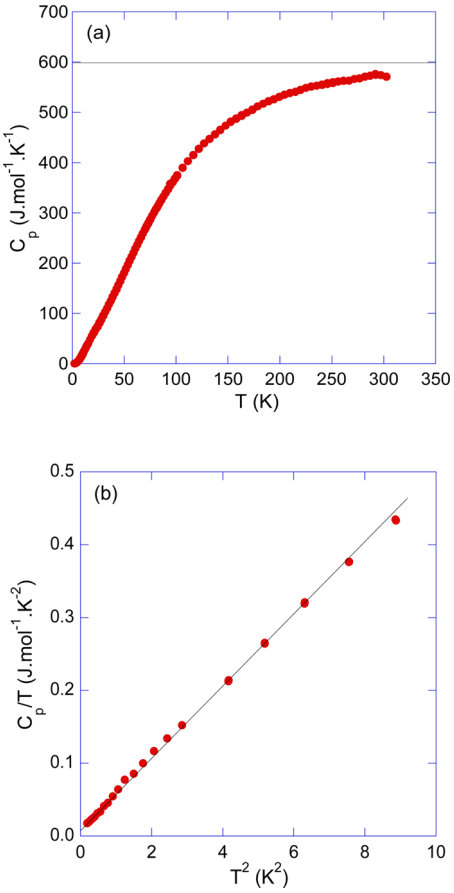

Figure 12. (a) Temperature dependence of the specific heat C_p. The solid black line stands for the Dulong–Petit value. (b) Low-temperature data plotted as C_p/T vs T^2. The solid black line is a guide to the eye to highlight the temperature range where a linear behavior is observed.

hand, numerical errors that accompany the determination of the position of the Fermi level may lead to a slight shift of E_F toward the band gap. Since the valence bands give rise to a strongly varying DOS region, a shift of E_F inside the bands would result in a finite γ value. On the other hand, the actual Ag and Tl contents might slightly differ from the titled stoichiometry thereby explaining the finite value of γ.

The β parameter is related to the Debye temperature θ_D via $\theta_D = ((12\pi^4 NR)/(5\beta))^{1/3}$ yielding $\theta_D \approx 100$ K. This extremely low value suggests a high degree of anharmonicity of the lattice vibrations. The situation is reminiscent to that observed in $Ag_xMo_9Se_{11}$ which shows a very low θ_D value and a pronounced curvature that scales with the Ag content.[22] This striking resemblance points to the presence of similar mechanisms responsible for this anharmonic behavior. In $Ag_xMo_9Se_{11}$, the local disorder associated with the Ag4 atoms (one of the four nonequivalent Ag sites) was considered as an indirect evidence of ionic conduction, even though this hypothesis should await for an experimental confirmation.[22] Our X-ray diffraction experiments have demonstrated the strong positional disorder of the Tl and, to a lesser extent, the Ag atoms. As mentioned earlier, in the type-I clathrates $Sr_8Ga_{16}Ge_{30}$ and $Eu_8Ga_{16}Ge_{30}$, the Sr and Eu atoms located in the tetrakaidecahedra are off-centered.[39−43] These atoms are distributed on an alternative 4-fold site in the cages with an occupation probability of 1/4. This peculiarity gives rise to anomalous thermal transport

dx.doi.org/10.1021/ic501939k | Inorg. Chem. 2014, 53, 11699−11709

including glass-like thermal conductivity and excess specific heat below 2 K.[42] These traits are observed in $Ag_2Tl_2Mo_9Se_{11}$ suggesting that the behavior of the Tl and Ag atoms parallel that of Sr and Eu atoms in clathrates. If this picture holds, both Tl and Ag might tunnel between local energy minima resulting in an additional contribution to C_p varying as $T^{1.2}$.[42] Interestingly, a fraction of the nonvanishing γ value might reflect these tunneling states. This scenario may be shown conclusively by the temperature dependence of the thermal conductivity, which should follow a T^2 law at very low temperatures (typically below ~1 K).[40,42]

Figure 13 presents the temperature dependence of the total thermal conductivity. The κ data show a glass-like behavior

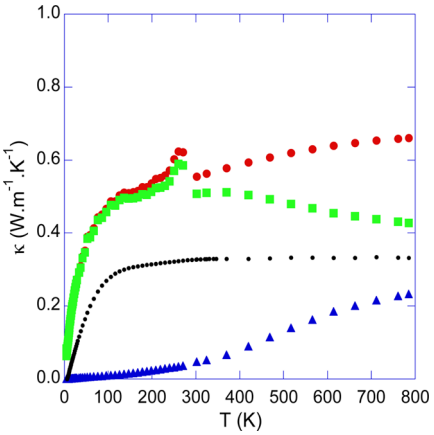

Figure 13. Temperature dependence of the total (red ●), lattice (green ■), and electronic (blue ▲) thermal conductivities. The slight upturns observed near 300 K are due to thermal radiations. The dotted black line stands for the temperature dependence of the minimum lattice thermal conductivity calculated from eq 2.

mainly characterized by the absence of low-temperature crystalline peak and very low values in the entire temperature range. To separate the electronic from the lattice contribution, we have estimated the former using the Wiedemann–Franz relation $\kappa_e = LT/\rho$ where L is the Lorenz number. Since the scattering mechanisms of charge carriers could not be determined from Hall effect data, L was assumed to be equal to 2.0×10^{-8} $V^2 \cdot K^{-2}$, a value typically found in heavily doped semiconductors. Subtracting κ_e from κ then leaves an estimation of the lattice thermal conductivity κ_L (see Figure 13). The κ_L values are very low in the whole temperature range and never exceed 0.5 $W \cdot m^{-1} \cdot K^{-1} \cdot \kappa_L$ is close to the minimum thermal conductivity κ_m given by[51]

$$\kappa_{min} = \left(\frac{\pi}{6}\right)^{1/3} k_B V^{-2/3} \sum_i \left[v_i \left(\frac{T}{\theta_i}\right)^2 \int_0^{\theta_i/T} \frac{x^3 e^x}{(e^x - 1)^2} dx \right] \quad (2)$$

where k_B is the Boltzmann constant, V is the atomic volume and v_i and θ_i are the group velocity and the Debye temperature of mode i, respectively. In eq 2, the sum is performed over one longitudinal and two transverse modes. The corresponding sound velocities v_L and v_S were determined experimentally from ultrasonic measurements to be equal to 3340 and 1665 $m \cdot s^{-1}$, respectively. This result indicates that the phonon mean free path l approaches its lowest value at high temperatures; that is, $l = \lambda/2$ for a phonon of wavelength λ.

To shed light on the physical mechanisms responsible for these extremely low κ_L values, the average-mode Grüneisen constant γ_G was estimated. This parameter represents a measure of the bonding anharmonicity and governs the phonon–phonon scattering rate, which is proportional to γ_G^2.[52] Large γ_G values are indicative of high anharmonicity and reflect stronger phonon scattering, that is, lower thermal conductivity values. γ_G is defined as $\gamma_G = 3(\beta B V_m)/(C_v) \approx 3(\beta B V_m)/(C_p)$ where B is the isothermal bulk modulus, V_m is the molar volume and C_v is the isochoric specific heat which can be taken, to a good approximation, to be equal to C_p. B was calculated from $B = \rho(v_L^2 - (4/3)v_S^2$ giving $B = 56.5$ GPa. The room-temperature C_p value together with $\beta = 9.3.10^{-6}$ K^{-1} (calculated as $(2\beta_a + \beta_c)/3$) then yields $\gamma \approx 0.9$. This value is lower than those found in PbTe ($\gamma = 1.45$), $AgSbTe_2$ ($\gamma = 2.05$) or $Cu_2Ga_{0.1}Ge_{0.9}Se_3$ ($\gamma = 1.7$) suggesting a moderate degree of anharmonicity.[53–56]

Dimensionless Thermoelectric Figure of Merit. The dimensionless thermoelectric figure of merit is shown in Figure 14 as a function of temperature. In the temperature range

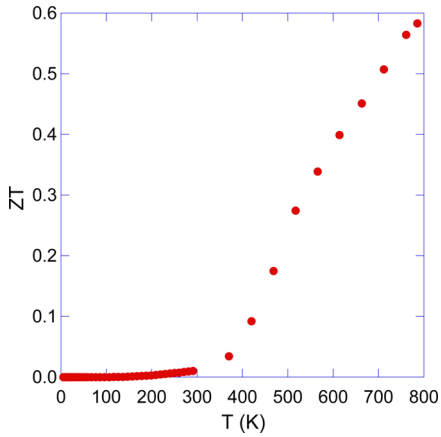

Figure 14. Temperature dependence of the dimensionless thermoelectric figure of merit ZT.

studied, a maximum ZT of 0.6 is reached at 800 K, a value comparable to those obtained in the $Ag_xMo_9Se_{11}$ and $Ag_3In_2Mo_{15}Se_{19}$ cluster compounds.[21–23] Further optimization might be achieved by adjusting the carrier concentration through substitutions or by varying the Ag and/or Tl concentrations.

■ CONCLUSION

We investigated the crystal structure from 300 down to 100 K, the electronic band structure and the transport properties between 2 and 800 K of the novel cluster compound $Ag_2Tl_2Mo_9Se_{11}$. The hexagonal unit cell is composed of Mo_9Se_{11} clusters between which, Ag and Tl atoms reside. DFT calculations have shown that, for the first time, metal–metal bonding within the Mo_9 bioctahedral cluster is optimized in this compound. Hall effect measurements revealed that both electrons and holes participate to the electrical conduction. This fact, consistent with the dispersion curves, may prove to be a feature shared by numerous families of Mo-based cluster compounds. Thermal transport is limited to its lowest possible value due to the local static disorder induced by the Tl and Ag atoms. A first experimental signature of the related low-lying phonon modes is provided by the low-temperature C_p data

dx.doi.org/10.1021/ic501939k | Inorg. Chem. 2014, 53, 11699–11709

governed by an extremely low Debye temperature. Owing to very low κ_L values, a relatively high ZT value of 0.6 was achieved at 800 K. Further optimization might be realized by varying the Ag/Tl ratio and by exploring possible substitutions onto the Mo and/or Se sites. On a more fundamental level, spectroscopic tools may help pinpoint the mechanism from which, such low κ_L values emerge thereby guiding the search of novel and efficient thermoelectric materials.

■ ASSOCIATED CONTENT

Supporting Information

Structure model used to perform the electronic band structure calculations. This material is available free of charge via the Internet at http://pubs.acs.org. Further details of the crystal structure investigation can be obtained from the Fachinformationszentrum Karlsruhe, 76344 Eggenstein-Leopoldshafen, Germany, (fax: (49) 7247−808−666; e-mail: crysdata@fiz.karlsruhe.de) on quoting the depository number CSD- 428026.

■ AUTHOR INFORMATION

Corresponding Author

*E-mail: patrick.gougeon@univ-rennes1.fr. Fax: +33 2 2323 6799.

Notes

The authors declare no competing financial interest.

■ ACKNOWLEDGMENTS

R.G. and P.G. are indebted to the Région Bretagne for a Ph.D. grant (R. A. R. A. O.). M.C. acknowledges the European Space Agency for financial support under NPI contract. Support from the Hubert Curien bilateral French-Czech Barrande project is also acknowledged. E. Santava is warmly thanked for specific heat measurements. J.H. acknowledges the technical aide of MLTL (see: http://mltl.eu), which is supported within the program of Czech Research Infrastructures (Project No. LM2011025).

■ REFERENCES

(1) Chevrel, R.; Sergent, M.; Pringent, J. *J. Solid State Chem.* **1971**, *3*, 515−519.

(2) Yvon, K. In *Current Topics in Material Science;* Kaldis, E., Ed.; North-Holland: Amsterdam, **1979**; Vol. *3*, p 53.

(3) Gougeon, P.; Potel, M.; Gautier, R. *Inorg. Chem.* **2004**, *43*, 1257−1263.

(4) Gougeon, P.; Padiou, J.; Lemarouille, J. Y.; Potel, M.; Sergent, M. *J. Solid State Chem.* **1984**, *51*, 218−226.

(5) Gougeon, P.; Potel, M.; Padiou, J.; Sergent, M. *Mater. Res. Bull.* **1987**, *22*, 1087−1093.

(6) Gautier, R.; Picard, S.; Gougeon, P.; Potel, M. *Mater. Res. Bull.* **1999**, *34*, 93−101.

(7) (a) Gougeon, P.; Potel, M.; Sergent, M. *Acta Crystallogr.* **1989**, *C45*, 182. (b) Gougeon, P.; Potel, M.; Sergent, M. *Acta Crystallogr.* **1989**, *C45*, 1413.

(8) Gougeon, P.; Potel, M.; Padiou, J.; Sergent, M. *Mater. Res. Bull.* **1988**, *23*, 453−460.

(9) Picard, S.; Gougeon, P.; Potel, M. *Acta Crystallogr.* **1997**, *C53*, 1519.

(10) Picard, S.; Gougeon, P.; Potel, M. *Angew. Chem.* **1999**, *38*, 2034−2036.

(11) Picard, S.; Saillard, J.-Y.; Gougeon; Noël, H. P.; Potel, M. *J. Solid State Chem.* **2000**, *155*, 417−426.

(12) Picard, S.; Halet, J.-F.; Gougeon, P.; Potel, M. *Inorg. Chem.* **1999**, *38*, 4422−4429.

(13) Gougeon, P.; Gall, P.; Gautier, R.; Potel, M. *Acta Crystallogr.* **2010**, *C66*, i67.

(14) Fischer, Ø. *Appl. Phys.* **1978**, *16*, 1−28.

(15) Petrovic, A. P.; Lortz, R.; Santi, G.; Berthod, C.; Dubois, C.; Decroux, M.; Demuer, A.; Antunes, A. B.; Paré, A.; Salloum, D.; Gougeon, P.; Potel, M.; Fischer, Ø. *Phys. Rev. Lett.* **2011**, *106*, 017003.

(16) Petrovic, A. P.; Lortz, R.; Santi, G.; Decroux, M.; Monnard, H.; Fischer, Ø.; Boeri, L.; Andersen, O. K.; Kortus, J.; Salloum, D.; Gougeon, P.; Potel, M. *Phys. Rev. B* **2010**, *82*, 235128.

(17) Tessema, G. X.; Tseng, Y. T.; Skove, M. J.; Stillwell, E. P.; Brusetti, R.; Monceau, P.; Potel, M.; Gougeon, P. *Phys. Rev. B* **1991**, *43*, 3434−3437.

(18) Brusetti, R.; Briggs, A.; Laborde, O.; Potel, M.; Gougeon, P. *Phys. Rev. B* **1994**, *49*, 8931−8943.

(19) Goldsmid, H. J. In *Thermoelectric Refrigeration;* Temple Press Books Ltd: London, U.K., 1964.

(20) Slack, G. A. *CRC Handbook of Thermoelectrics;* Rowe, D. M., Ed.; CRC: Boca Raton, FL, 1995; p 407.

(21) Zhou, T.; Lenoir, B.; Colin, M.; Dauscher, A.; Gall, P.; Gougeon, P.; Potel, M.; Guilmeau, E. *Appl. Phys. Lett.* **2011**, *98*, 162106.

(22) Zhou, T.; Colin, M.; Candolfi, C.; Boulanger, C.; Dauscher, A.; Santava, E.; Hejtmanek, J.; Baranek, P.; Al Rahal Al Orabi, R.; Potel, M.; Fontaine, B.; Gougeon, P.; Gautier, R.; Lenoir, B. *Chem. Mater.* **2014**, *26*, 4765−4775.

(23) Gougeon, P.; Gall, P.; Al Rahal Al Orabi, R.; Fontaine, B.; Gautier, R.; Potel, M.; Zhou, T.; Lenoir, B.; Colin, M.; Candolfi, C.; Dauscher, A. *Chem. Mater.* **2012**, *24*, 2899−2908.

(24) Yamanaka, S.; Kurosaki, K.; Kosuga, A.; Goto, K.; Muta, H. *MRS Symp. Proc.* **2006**, *886*, 337−341.

(25) Kurosaki, K.; Kosuga, A.; Muta, H.; Uno, M.; Yamanaka, S. *Appl. Phys. Lett.* **2005**, *87*, 061919.

(26) Wolfing, B.; Kloc, C.; Teubner, J.; Bucher, E. *Phys. Rev. Lett.* **2001**, *86*, 4350−4353.

(27) Gougeon, P.; Gall, P.; Potel, M. *Acta Crystallogr.* **2010**, *E66*, i56.

(28) Nonius, B. V. *COLLECT*, data collection software; Nonius BV: Delft, The Netherlands, 1999.

(29) Duisenberg, A. J. M. Ph.D. Thesis, University of Utrecht: Utrecht, The Netherlands, 1998.

(30) de Meulenaer, J.; Tompa, H. *Acta Crystallogr., Sect. A: Found. Crystallogr.* **1965**, *19*, 1014−1018.

(31) Altomare, A.; Burla, M. C.; Camalli, M.; Cascarano, G. L.; Giacovazzo, C.; Guagliardi, A.; Moliterni, A. G. G.; Polidori, G.; Spagna, R. *J. Appl. Crystallogr.* **1999**, *32*, 115−119.

(32) Sheldrick, G. M. *Acta Crystallogr., Sect. A* **2008**, *64*, 112−122.

(33) (a) Andersen, O. K. *Phys. Rev. B* **1975**, *12*, 3060−3083. (b) Andersen, O. K. *Europhys. News* **1981**, *12*, 4−8. (c) Andersen, O. K. In *The Electronic Structure Of Complex Systems;* Phariseau, P., Temmerman, W. M., Eds.; Plenum Publishing Corporation: New York, 1984;. (d) Andersen, O. K.; Jepsen, O. *Phys. Rev. Lett.* **1984**, *53*, 2571−2574. (e) Andersen, O. K.; Jepsen, O.; Sob, M. In *Electronic Band Structure and its Application;* Yussouf, M., Ed.; Springer-Verlag: Berlin, Germany, 1986. (f) Skriver, H. L. *The LMTO Method;* Springer-Verlag: Berlin, Germany, 1984.

(34) von Barth, U.; Hedin, L. *J. Phys. C* **1972**, *5*, 1629−1642.

(35) Jepsen, O.; Andersen, O. K. *Z. Phys. B* **1995**, *97*, 35−47.

(36) Blöchl, P. E.; Jepsen, O.; Andersen, O. K. *Phys. Rev. B* **1994**, *49*, 16223−16233.

(37) Dronskowski, R.; Blöchl, P. E. *J. Phys. Chem.* **1993**, *97*, 8617−8624.

(38) Schäfer, H.; Von Schnering, H. G. *Angew. Chem.* **1964**, *20*, 833−849.

(39) Chakoumakos, B. C.; Sales, B. C.; Mandrus, D. G. *J. Alloys Compd.* **2001**, *322*, 127−134.

(40) Paschen, S.; Carrillo-Cabrera, W.; Bentien, A.; Tran, V. H.; Baenitz, M.; Grin, Yu.; Steglich, F. *Phys. Rev. B* **2001**, *64*, 214404.

(41) Xu, J.; Tang, J.; Sato, K.; Tanabe, Y.; Miyasaka, H.; Yamashita, M.; Heguri, S.; Tanigaki, K. *Phys. Rev. B* **2010**, *82*, 085206.

(42) Umeo, K.; Avila, M. A.; Sakata, T.; Suekuni, K.; Takabatake, T. *J. Phys. Soc. Jpn.* **2005**, *74*, 2145−2148.

(43) Sales, B. C.; Chakoumakos, B. C.; Jin, R.; Thompson, J. R.; Mandrus, D. *Phys. Rev. B* **2001**, *63*, 245113.
(44) These electrons are located in MOs that are mainly metallic in character. Among these electrons, some of them are responsible for metal−metal bonding. Assuming an ionic bonding picture between oxidized metal atoms and anionic surrounding ligands, this ME count is obtained by adding the remaining number of valence electrons of the oxidized metal atoms in their actual oxidation states.
(45) Gautier, R.; Gougeon, P.; Halet, J.-F.; Potel, M.; Saillard, J.-Y. *J. Alloys Compd.* **1997**, *262*−*263*, 311−315.
(46) Fenske, D.; Ohmer, J.; Hachgenei, J. *Angew. Chem., Int. Ed. Engl.* **1985**, *24*, 993−995.
(47) Gautier, R.; Furet, E.; Halet, J.-F.; Lin, Z.; Saillard, J.-Y; Xu, Z. *Inorg. Chem.* **2002**, *41*, 796−804.
(48) Salloum, D.; Gautier, R.; Gougeon, P.; Potel, M. *J. Solid State Chem.* **2004**, *177*, 1672−1680.
(49) Salloum, D.; Gougeon, P.; Potel, M.; Gautier, R. *C. R. Chim.* **2005**, *8*, 1743−1749.
(50) See, for example, Askerov, B. M. In *Electron Transport Phenomena in Semiconductors;* World Scientific Publishing Ltd.: Singapore, 1994.
(51) Cahill, D. G.; Watson, S. K.; Pohl, R. O. *Phys. Rev. B* **1992**, *46*, 6131−6140.
(52) Ganesan, S. *Philos. Mag.* **1962**, *7*, 197−205.
(53) Clasen, R.; Harbeke, G.; Krost, A.; Levy, F.; Madelung, O.; Maschke, K.; Nimtz, G.; Schlicht, B.; Schmitte, F. J. *Physics of Non-Tetrahedrally Bonded Binary Compounds II,* Landolt-Börnstein Numerical Data and Functional Relationships in Science and Technology, Group III; Madelung, O., Ed.; Springer: Berlin, Germany, 1983; Vol. *17*, Subvolume *f*, p 419, Figure 18.
(54) Slack, G. A. In *Solid State Physics;* Ehrenreich, H., Weitz, F., Turnbull, D., Eds.; Academic Press: New York, 1979; Vol. *34*, pp 1−71.
(55) Cho, J. Y.; Shi, X.; Salvador, J. R.; Meisner, G. P.; Yang, J.; Wang, H.; Wereszczak, A. A.; Zhou, X.; Uher, C. *Phys. Rev. B* **2011**, *84*, 085207.
(56) Nielsen, M. D.; Ozolins, V.; Heremans, J. P. *Energy Environ. Sci.* **2013**, *6*, 570−578.